ChemPubSoc Europe

DOI: 10.1002/celc.201700590

CHEMELECTROCHEM Articles

Intertwined Nitrogen-Doped Carbon Nanotubes for High-Rate and Long-Life Sodium-Ion Battery Anodes

Kang Ding,[a] Biao Gao,*[a] Jijiang Fu,[a] Weili An,[a] Hao Song,[a] Xingxing Li,[a] Qiuyun Yuan,[a] Xuming Zhang,[a] Kaifu Huo,*[b] and Paul K. Chu[c]

Intertwined nitrogen-doped carbon nanotubes (N-CNTs) are prepared by using a hard-template method with V_2O_5 nanowires as the hard template and dopamine as the carbon and nitrogen source, and the N-CNTs are characterized in details. As anodes in sodium-ion batteries (SIBs), the N-CNTs deliver a capacity of 179.1 mAh g^{-1} at 0.2 A g^{-1}, and a capacity of 91.7 mAh g^{-1} is maintained even at 10 A g^{-1}. After cycling for 1000 cycles at 1 and 5 A g^{-1}, the capacity of the N-CNTs is retained at 125.5 and 104.2 mAh g^{-1}, respectively. The excellent electrochemical performance in terms of rate capability and lifespan of the N-CNTs can be attributed to the synergistic effects of the intertwined one-dimensional hollow structure with hierarchical pores, extrinsic nitrogen content, and large interlayer distance of the graphene sheets.

1. Introduction

Lithium-ion batteries (LIBs) are one of the most common energy sources for electric vehicles, portable devices, and energy storage devices.[1] However, the relatively high price and uneven geological distribution of natural lithium reserve raise uncertainty about the long-term sustainability of the technology.[2] Sodium-ion batteries (SIBs) have several advantages over LIBs in next-generation energy storage devices due to the abundance and low cost. Nevertheless, SIBs generally suffer from the poor stability and slow mass transport due to the large radius of sodium ions (~34% larger than that of lithium ion)[3] and low energy density caused by the reduced operating voltage (negative redox potential of Na^+/Na is −2.71 V *vs* SHE and 0.33 V higher than that of Li).[4] Designing the suitable electrode materials with high reversibility in Na^+ insertion/extraction, enhancing the ability against deformation of volume, and improving the conductivity are the research focus to overcome the limited performance of SIBs. Compared to the extensive study on cathodes in SIBs, there have been less research activities on anodes with high capacity, durability, and good rate performance.

Recently, metal oxides/sulfides/nitrides,[3,5] metal alloys,[6] phosphorous[7] and carbonaceous materials[8] have been shown as promising anode materials in SIBs. Among them, non-graphitized carbon materials have attracted much attention because of the disordered structure with a larger interlayer distance as well as low cost.[2b] Carbonaceous materials with various morphologies and structures have been reported, for example, carbon nano/microspheres,[2a,9] carbon nanofibers,[10] carbon nanosheets[11] and biomass-derived carbon.[12] However, there are still technical obstacles in order to make carbonaceous materials desirable as anodes in SIBs. First of all, the large volume change during the Na^+ insertion/extraction process causes structural alteration during extended cycling resulting in unsatisfactory lifetime for carbon-based anodes. Secondly, carbon-based anodes often suffer from low rates due to low graphitization,[13] long ion transport distance, and low solid-state diffusion coefficient of sodium ions.[12a] In order to improve the rate performance and stability, new structures are needed.

Hollow carbon architectures such as hollow spheres,[2a] open-end carbon nanotubes[14] and nanocages[15] provide the necessary space enabling good cycling stability characteristics. Compared to carbon hollow spheres and nanocages, open-end carbon nanotubes with a one-dimensional morphology and large aspect ratio can potentially deliver excellent electrochemical performance in SIBs due to the one-dimensional electron transfer channel and hierarchical porous system. Cao et al. synthesized hollow carbon nanowires by annealing a hollow polyaniline nanowire precursor and the product showed a considerable capacity retention of 82.2% after 400 charging-discharging cycles[16] and Li et al fabricated bamboo-like carbon nanotubes with high capacity and superior stability.[14] Among the various modification methods, nitrogen doping has been shown to enhance the capacity and rate capability as a result of the improved electron conductivity, reactivity, and sodium adsorption through the generation of extrinsic defects.[11a,17] Huang et al. produced functionalized N-doped interconnected

[a] K. Ding, Dr. B. Gao, Prof. J. Fu, W. An, H. Song, X. Li, Q. Yuan, Prof. X. Zhang
The State Key Laboratory of Refractories and Metallurgy
Wuhan University of Science and Technology
Wuhan 430081, China
E-mail: gaobiao@wust.edu.cn
[b] Prof. K. Huo
Wuhan National Laboratory for Optoelectronics (WNLO)
School of Optical and Electronic Information
Huazhong University of Science and Technology
Wuhan 430074, China
E-mail: kfhuo@hust.edu.cn
[c] Prof. P. K. Chu
Department of Physics and Materials Science
City University of Hong Kong
Tat Chee Avenue, Kowloon, Hong Kong, China

Supporting information for this article is available on the WWW under https://doi.org/10.1002/celc.201700590

carbon nanofibers as anodes in SIBs which delivered a specific capacity of 73 mAh g^{-1} even at 20 A g^{-1}.[17] Lou et al. demonstrated a electrospinning strategy to fabricate nitrogen-doped carbon nanofibers with a high capacity of 210 mAh g^{-1} at 5 A g^{-1}.[18]

Herein, we describe the fabrication of intertwined nitrogen-doped carbon nanotubes (N-CNTs) derived from dopamine by a hard template method. The N-CNTs have several advantages as anodes in SIBs. First of all, the hollow structure with an ultrathin (~10 nm) and porous shell not only buffers the volumetric change during Na ion insertion/extraction, but can also increases the active sites and electrode/electrolyte interface. Secondly, the N-CNTs with a large aspect ratio (~100 nm in diameter and ~30 μm in length) can assemble into a 3D hierarchical porous system to facilitate Na ion transport. Thirdly, N atoms in the N-CNTs improve the capacity and the rate performance of the carbon-based electrodes by enhancing the conductivity, reactivity, and sodium adsorption. As a result, as an anode in SIBs, the N-CNTs deliver a high capacity of 179.1 mAh g^{-1} at 0.2 A g^{-1} (0.54 C, 1 C = 0.372 A g^{-1}) and exhibit good stability even after 1,000 cycles at 1 A g^{-1} (2.7 C) and 5 A g^{-1} (13.4 C). Moreover, a capacity of 91.7 mAh g^{-1} is maintained even at a high rate of 10 A g^{-1} (27 C).

2. Results and Discussion

The schematic illustration of the synthetic procedure is exhibited in Figure 1a. The V_2O_5 NWs with a diameter ~100 nm

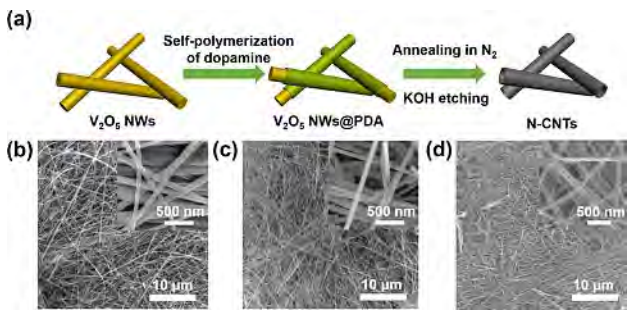

Figure 1. a) Schematic illustration of the synthesis of the N-CNTs; SEM images of b) V_2O_5 NWs, c) V_2O_5@PDA NWs, and d) N-CNTs. The insets of (b)–(d) show the magnified images of the V_2O_5 NWs, V_2O_5@PDA NWs, and N-CNTs, respectively.

and length of tens of micrometers (Figure 1b with the inset being the magnified image) are coated with a polydopamine (PDA) layer by chemical polymerization. The PDA-coated V_2O_5 NWs (V_2O_5@PDA NWs) retain the 1D morphology (Figure 1) with the inset being the magnified image). The XRD patterns of V_2O_5@PDA can be indexed to orthorhombic V_2O_5 (JCPDS Card No. 89-0612) which is the same as the pristine V_2O_5 NWs, as shown in Figures S1(a) and S1(b). After the V_2O_5@PDA NWs are annealed in N_2, the core of V_2O_5 NWs is reduced to V_2O_3 (JCPDS Card No. 34-0187) while the PDA shell is pyrolyzed into carbon producing the carbon-coated V_2O_3 (V_2O_3@C) nanowires (XRD pattern and SEM image depicted in Figure S1(c) and Figure S2). The V_2O_3@C nanowires are then dissolved in KOH to remove the V_2O_3 core to obtain the N-CNTs. The 1D structure is inherited except that the length shortens (~30 μm) after annealing and etching, and the tubes intertwine to form a 3D web structure, as shown in Figure 1d.

The tube-like structures have a diameter of ~100 nm and wall thickness of ~10 nm as shown in Figures 2a and 2b. The

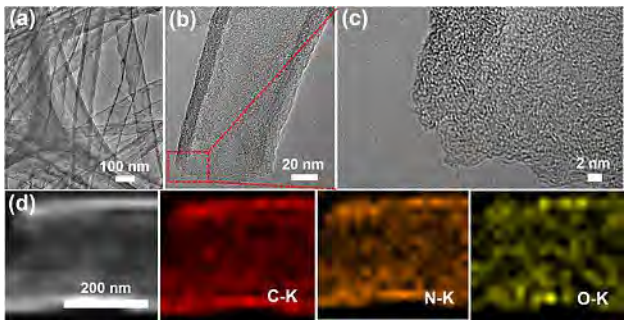

Figure 2. a, b) TEM and c) corresponding HR-TEM images of the N-CNTs; d) carbon, nitrogen, and oxygen elemental maps in the N-CNTs.

ultrathin wall shortens the sodium ion diffusion distance. Moreover, a turbostratic structure is observed by the high-resolution TEM (HR-TEM) as shown in Figure 2c indicating the amorphous nature of the N-CNTs. The elemental maps in Figure 2d show that carbon, nitrogen, and oxygen are uniformly distributed in the tube and nitrogen incorporation into the carbon matrix. As shown in Figure 3a, two peaks at

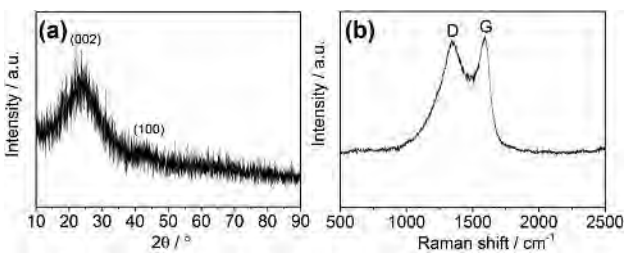

Figure 3. a) XRD pattern and b) Raman scattering spectrum of the N-CNTs.

23.7° and 43.5° are observed from the XRD pattern of the N-CNTs. The former one corresponds to the (002) plane and the layer distance of the (002) plane (d_{002}) calculated by Bragg's law is 0.375 nm which is larger than that of graphite (0.336 nm). This ensures effective Na-ion insertion into the N-CNTs.[16] Figure 3b displays Raman spectrum of the N-CNTs revealing D-band at around 1350 cm^{-1} and G-band at around 1590 cm^{-1} of carbon materials, respectively. The former is related to defects and disordered portions and the latter is associated with the ordered graphitic structure.[19] The intensity ratio of the D-band to G-band (I_D/I_G) is 0.976 suggesting partial destruction of the graphite structure being consistent with the HR-TEM and XRD results. The disordered turbostratic carbon structure with a

large interlayer spacing benefits reversible storage of the large sodium ions.[11a]

Nitrogen adsorption/desorption is monitored to investigate the specific surface area and pore size distribution of the N-CNTs. The BET specific surface area is calculated to be 736.9 $m^2 g^{-1}$. A reversible hysteresis loop at the relative pressure ranging from 0.5 to 0.95 in Figure 4a typically indicates that

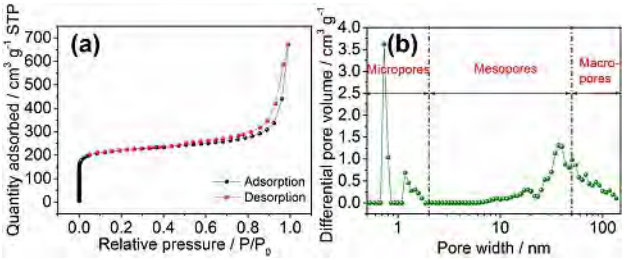

Figure 4. a) N_2 adsorption and desorption isotherms and b) pore-size distribution of the N-CNTs.

mesopores exist in the N-CNTs. The abrupt trend at low pressure shows that there is also a large amount of micropores. A distinctive hierarchical pore structure can be observed from the pore size distribution plots (Figure 4b). The micropores with sizes of 0.7–0.8 nm and 1–2 nm may arise from the release of water and gas during the carbonization process of PDA.[20] Nevertheless, the pores in the region of mesopores and even macropores do not necessarily originate from a single N-CNT but rather from the arrangement of the intertwined nanotube web. The N-CNTs with a large specific surface area and hierarchical pore distribution provide abundant active sites and sodium ion transport channels boding well for anodes in SIBs.[21]

According to the survey spectrum in Figure 5a, carbon, nitrogen, and oxygen exist on the as-prepared N-CNTs consis-

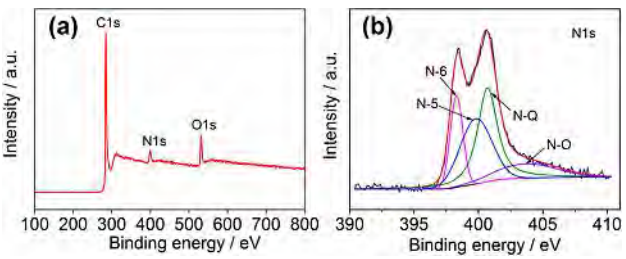

Figure 5. a) XPS survey spectrum and b) N 1s spectrum of the N-CNTs.

tent with the elemental maps. The concentration of nitrogen is as large as 5 at.%. The C1s spectrum in Figure S3 is divided into four sub-peaks. The peak located at 284.5 eV arises from sp^3 bonding and that at 285.4 eV can be ascribed to functional groups (C–OH) in the N-CNTs[17] in agreement with the FTIR results (Figure S4). The peaks at 285.7 and 287.5 eV are attributed to N-sp^2 C and N-sp^3 C, respectively.[11b] Four sub-peaks at 398.3, 399.8, 400.7, and 403.7 eV of the N1s spectrum are shown in Figure 5b in accordance with pyridinic N (N-6), pyrrolic or pyridonic N (N-5), and quaternary N (N–Q) as well as N–O, respectively.[14,22] The introduction of nitrogen can not only improve the conductivity of N-CNTs but also enhance the reactivity and sodium adsorption by generating extrinsic defects.[11a,17]

The cyclic voltammetry (CV) of the N-CNT anode is conducted between 0.001-3 V at a scanning rate of 0.2 mV s^{-1}, as shown in Figure 6a. In the first cathodic scan, a sharp

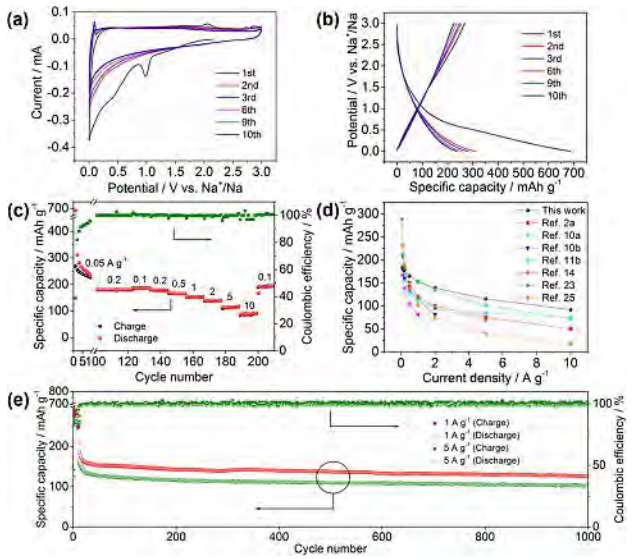

Figure 6. Electrochemical performance of the N-CNTs: a) cyclic voltammograms in the range of 0.001-3 V vs. Na^+/Na at a scanning rate of 0.2 mV s^{-1}; b) galvanostatic discharging-charging profiles at 0.05 A g^{-1}; c) rate performance of the N-CNTs; d) comparison of the rate capability between the N-CNTs and other carbonaceous materials; e) cycling performance of the N-CNTs at 1 and 5 A g^{-1}.

reduction peak emerges at 1.0 V indicating that the electrolyte reacts with surface functional groups of the electrode.[10a,23] The peak disappears during subsequent cycles implying irreversibility of this reaction. The electrolyte decomposes and the solid electrolyte interphase (SEI) forms in accordance with the relatively broad peak located at 0.5 V[23] which accounts for the majority of the irreversible capacity. The sharp peak at 0 V in the cathodic process corresponds to sodium ion insertion into the N-CNTs. In the anodic process, a peak at 0.1 V is observed due to extraction of Na ions from the N-CNTs.[2a,23] In the first cycle, the weak peaks at 2 V can be assigned to the redox reactions on surface of the functionalized carbon.[24] The CV curves acquired at 9th and 10th cycles overlap indicative of a stable SEI layer and reversible Na ion insertion/extraction. The Galvanostatic charging-discharging profiles of the N-CNTs are shown in Figure 6b. The initial discharging and charging capacities are 687.2 mAh g^{-1} and 268.6 mAh g^{-1} at 0.05 A g^{-1}, respectively, with the first coulombic efficiency being 39%. The large capacity loss stems from decomposition of the electrolyte, formation of the SEI layer, as well as the reaction between the electrolyte and functional groups being consistent with the CV results.[10a] As the materials are cycled, the capacity is

dominated by the sloping regions of the charge-discharge curves possibly due to insertion of sodium into the graphene layers of turbostratic carbon.[18]

The rate performance of the N-CNTs is presented in Figure 6c. The activation and stabilizing processes are conducted at 0.05 $A g^{-1}$ for the first 11 cycles and 0.2 $A g^{-1}$ for 111 cycles afterwards, giving a specific capacity of 179.1 $mAh g^{-1}$. The N-CNTs show reversible capacities of 185.3, 177.4, 165.1, 153.1, 138.9 and 115.3 $mAh g^{-1}$ at 0.1, 0.2, 0.5, 1, 2, and 5 $A g^{-1}$, respectively. Moreover, the specific capacity is maintained at 91.7 $mAh g^{-1}$ even at 10 $A g^{-1}$. As the rate diminishes to 0.1 $A g^{-1}$, a specific capacity of 192.4 $mAh g^{-1}$ can be recovered, displaying high reversibility. The rate capacity of commercial CNTs is also evaluated for comparison (Figure S6) and the capacities at the same current density are lower than those of the N-CNTs. The SEM image and Nyquist plot of commercial CNTs are also shown in Figure S5 and Figure S7(b), respectively. Moreover, the rate capability is superior to that of other reported carbonaceous nanostructures such as carbon nanospheres,[2a] carbon nanofibers,[10] carbon nanosheets,[11b] bamboo-like carbon nanotubes[14] and other carbonaceous materials[23, 25] as shown in Figure 6d. The outstanding rate performance delivered by the N-CNTs stems from the synergistic effects of the unique structure and nitrogen doping. First of all, the network consisting of the 3D intertwined 1D N-CNTs with a hierarchical porous structure guarantees both efficient sodium ion transport and electron conductivity. Secondly, the large interlayer spacing of the N-CNTs enables fast insertion/extraction of Na ions. Thirdly, the ultrathin walls of the N-CNTs reduce the diffusion pathway of Na ions and increase the availability of the materials especially at a large current density. Fourthly, nitrogen doped at a large concentration enhances the electron transport ability.

Figure 6e and Figure S7(a) show the cycle stability of the N-CNTs. Stabilization is conducted at 0.05 $A g^{-1}$ for the first 11 cycles in all cycle processes. As exhibited in Figure S7(a), the N-CNTs delivers a high discharge capacity of 166.02 $mAh g^{-1}$ after 200 cycles at 0.5 $A g^{-1}$. Furthermore, the Nyquist plots of the N-CNTs before and after different cycles at 0.5 $A g^{-1}$ are also demonstrated in Figure S7(b). The cycled Nyquist plots show two semicircles, representing the resistance of Na^+ transport through SEI (R_f) and charge transfer at the interface of electrolyte and SEI layer (R_{ct}). An increase in $R_f + R_{ct}$ compared with the initial R_{ct} indicates the disintegration of the N-CNTs to some extent.[12b] Moreover, the Nyquist plots at the 80th and the 130th cycle almost overlap, consistent with the good cycle stability of the N-CNTs in Figure S7(a). Figure 6e shows the cycle performance of the N-CNTs at high rates. A discharge capacity is maintained at 125.5 $mAh g^{-1}$ at 1 $A g^{-1}$ even after 1,000 cycles thus demonstrating high capacity and long-term stability. Furthermore, a high capacity of 104.2 $mAh g^{-1}$ is delivered by the N-CNTs electrode even at 5 $A g^{-1}$ after 1,000 cycles. Moreover, the coulombic efficiency of the N-CNTs anode reaches nearly 100% at 1 and 5 $A g^{-1}$. The outstanding stability of the N-CNTs anode can be ascribed to the special open-end and hollow one-dimensional structure and micropores in the wall, which can synergistically accommodate the volume variations in the Na ions insertion/extraction process. As demonstrated in Figure S8, the morphology of the N-CNTs electrode film does not change after 1,000 cycles at 1 $A g^{-1}$ indicating durability and robustness.

3. Conclusions

N-CNTs with a diameter of ~100 nm and wall thickness of ~10 nm are prepared by dopamine polymerization with V_2O_5 NWs as the template. The N-CNTs have a large nitrogen concentration of 5 at.%, large interlayer spacing, and hierarchical pores consisting of micropores, mesopores and macropores, thus producing desirable effects such as more abundant active sites, accelerated Na ion transport, and buffering of volumetric expansion during Na ions insertion. As SIBs anode, the N-CNTs have a high capacity of 179.1 $mAh g^{-1}$ at 0.2 $A g^{-1}$ and show outstanding rate performance with a considerable capacity of 91.7 $mAh g^{-1}$ at 10 $A g^{-1}$. Excellent cycling stability is also observed as demonstrated by the capacities of 125.5 and 104.2 $mAh g^{-1}$ after 1,000 cycles at 1 and 5 $A g^{-1}$, respectively. These results suggest that the N-CNTs are excellent anode materials in SIBs.

Experimental Section

Synthesis of the N-CNTs

The N-CNTs were fabricated by a hard template method with V_2O_5 nanowires (V_2O_5 NWs) as the template according to the method described by Zhai et al.[26] 100 mg of V_2O_5 NWs were homogeneously dispersed in 100 mL of distilled water and 121 mg of Tris and 120 mg of dopamine (DA) were added in succession and stirred at 25 °C in air for 1 h. The black dispersion was washed and filtered to obtain the dark green products. After vacuum freeze-drying for a day, the products were heated at 400 °C for 30 min with a ramping rate of 2 °C min^{-1} and then at 700 °C for 3 h with a heating rate of 5 °C min^{-1} under a nitrogen flow. The annealed black products were dissolved in 0.5 M KOH at 50 °C until the templates were completely etched. Finally, the N-CNTs were obtained after washing with distilled water three times and freeze-drying.

Materials Characterization

The structure and morphology of the samples were characterized by field-emission scanning electron microscopy (FE-SEM, FEI Nova 450 Nano), transmission electron microscopy (HR-TEM, FEI Titan G2 60-300), X-ray diffraction using Cu Kα radiation ($\lambda = 1.5418$ Å) (XRD, Philips X' Pert Pro) and Raman scattering (HR RamLab) with the 514.5 nm Ar^+ laser as the excitation source. Elemental analysis was performed by X-ray photoelectron spectroscopy (XPS, ESCALab250) and FTIR spectra were collected on the IFS-85 (Bruker) spectrometer. The nitrogen adsorption and desorption isotherms were obtained by nitrogen physisorption at 77 K on a Micrometritics ASAP 2020 analyzer.

Electrochemical Characterization

The electrode was produced by mixing the N-CNTs, sodium alginate, and acetylene black at a weight ratio of 8:1:1. Distilled water was used to dissolve the binder. A slurry was prepared and coated on copper foil and finally vacuum dried at 75 °C for 12 h. The mass loading of active material on the electrode is about 0.9 mg cm^{-2}. The cell (CR2032) was assembled using a glove box under argon with oxygen and water being less than 0.1 ppm. The sodium plate, Whatman glass fiber, and 1 M $NaClO_4$ in propylene carbonate (PC) and ethylene carbonate (EC) mixture solution (1:1 volume ratio) were used as counter electrode, separator, and electrolyte, respectively. Cyclic voltammetry was conducted using an electrochemical workstation (CHI760e, Shanghai Chenhua Instrument Co., Ltd.) and the scanning rate was 0.2 mV s^{-1}. Electrochemical impedance measurements were also performed on the same electrochemical workstation in the frequency range from 100 kHz to 0.01 Hz, and the voltage perturbation was controlled at 5 mV. Galvanostatic charging–discharging (0.001–3 V) tests were performed on an LANT CT2001 battery test system at room temperature.

Acknowledgements

This work was financially supported by National Natural Science Foundation of China (51504171 and 51572100), Project of Hubei Provincial Education Office (B2015346), Outstanding Young and Middle-aged Scientific Innovation Team of Colleges and Universities of Hubei Province (T201402), Applied Basic Research Program of Wuhan City (2013011801010598), Project of Natural Science Foundation of Hubei Province (2015CFA116), and City University of Hong Kong Applied Research Grant (ARG, No. 9667122).

Conflict of Interest

The authors declare no conflict of interest.

Keywords: sodium-ion batteries · carbon anodes · nanotubes · doping · dopamines

[1] a) X. Li, J. Fu, Z. Pan, J. Su, J. Xu, B. Gao, X. Peng, L. Wang, X. Zhang, P. K. Chu, *J. Power Sources* **2016**, *331*, 58–66; b) W. An, J. Fu, J. Su, L. Wang, X. Peng, K. Wu, Q. Chen, Y. Bi, B. Gao, X. Zhang, *J. Power Sources* **2017**, *345*, 227–236; c) S. Zheng, X. Li, B. Yan, Q. Hu, Y. Xu, X. Xiao, H. Xue, H. Pang, *Adv. Energy Mater.* **2017**, *1602733*; d) Y. Yan, B. Li, W. Guo, H. Pang, H. Xue, *J. Power Sources* **2016**, *329*, 148–169.

[2] a) K. Tang, L. Fu, R. J. White, L. Yu, M. M. Titirici, M. Antonietti, J. Maier, *Adv. Energy Mater.* **2012**, *2*, 873–877; b) D. Xu, C. Chen, J. Xie, B. Zhang, L. Miao, J. Cai, Y. Huang, L. Zhang, *Adv. Energy Mater.* **2016**, *6*, 1501929.

[3] L. Wang, J. Sun, R. Song, S. Yang, H. Song, *Adv. Energy Mater.* **2016**, *6*, 1502067.

[4] T. Ramireddy, M. M. Rahman, N. Sharma, A. M. Glushenkov, Y. Chen, *J. Power Sources* **2014**, *271*, 497–503.

[5] a) L. David, R. Bhandavat, G. Singh, *ACS Nano* **2014**, *8*, 1759–1770; b) S. Hariharan, K. Saravanan, P. Balaya, *Electrochem. Commun.* **2013**, *31*, 5–9.

[6] S. Liu, J. Feng, X. Bian, J. Liu, H. Xu, *Energ. Environ. Sci.* **2016**, *9*, 1229–1236.

[7] J. Sun, H. W. Lee, M. Pasta, H. Yuan, G. Zheng, Y. Sun, Y. Li, Y. Cui, *Nat. Nanotechnol.* **2015**, *10*, 980–985.

[8] D. A. Stevens, J. R. Dahn, *J. Electrochem. Soc.* **2000**, *147*, 1271–1273.

[9] Y. Li, Z. Wang, L. Li, S. Peng, L. Zhang, M. Srinivasan, S. Ramakrishna, *Carbon* **2016**, *99*, 556–563.

[10] a) L. Fu, K. Tang, K. Song, P. A. van Aken, Y. Yu, J. Maier, *Nanoscale* **2014**, *6*, 1384–1389; b) T. Chen, Y. Liu, L. Pan, T. Lu, Y. Yao, Z. Sun, D. C. Chua, Q. Chen, *J. Mater. Chem. A* **2014**, *2*, 4117–4121.

[11] a) H. Wang, Z. Wu, F. Meng, D. Ma, X. Huang, L. Wang, X. Zhang, *ChemSusChem* **2013**, *6*, 56–60; b) F. Yang, Z. Zhang, K. Du, X. Zhao, W. Chen, Y. Lai, J. Li, *Carbon* **2015**, *91*, 88–95.

[12] a) Y. Li, Y. Hu, M. M. Titirici, L. Chen, X. Huang, *Adv. Energy Mater.* **2016**, *6*, 1600659; b) J. Ding, H. Wang, Z. Li, A. Kohandehghan, K. Cui, Z. Xu, B. Zahiri, X. Tan, E. M. Lotfabad, B. C. Olsen, *ACS Nano* **2013**, *7*, 11004–11015.

[13] Y. Yan, Y. Yin, Y. Guo, L. Wan, *Adv. Energy Mater.* **2014**, *4*, 1079–1098.

[14] D. Li, L. Zhang, H. Chen, L. Ding, S. Wang, H. Wang, *Chem. Commun.* **2015**, *51*, 16045–16048.

[15] Z. Lyu, L. Yang, D. Xu, J. Zhao, H. Lai, Y. Jiang, Q. Wu, Y. Li, X. Wang, Z. Hu, *Nano Res.* **2015**, *8*, 3535–3543.

[16] Y. Cao, L. Xiao, M. L. Sushko, W. Wang, B. Schwenzer, J. Xiao, Z. Nie, L. V. Saraf, Z. Yang, J. Liu, *Nano Lett.* **2012**, *12*, 3783–3787.

[17] Z. Wang, Q. Long, L. Yuan, W. Zhang, X. Hu, Y. Huang, *Carbon* **2013**, *55*, 328–334.

[18] S. Wang, L. Xia, L. Yu, L. Zhang, H. Wang, X. Lou, *Adv. Energy Mater.* **2016**, *6*, 1502217.

[19] J. Xu, M. Wang, N. P. Wickramaratne, M. Jaroniec, S. Dou, L. Dai, *Adv. Mater.* **2015**, *27*, 2042–2048.

[20] F. Leroux, C. Taviot-Guého, *J. Mater. Chem.* **2005**, *15*, 3628–3642.

[21] a) W. Li, L. Zeng, Z. Yang, L. Gu, J. Wang, X. Liu, J. Cheng, Y. Yu, *Nanoscale* **2014**, *6*, 693–698; b) W. Luo, J. Schardt, C. Bommier, B. Wang, J. Razink, J. Simonsen, X. Ji, *J. Mater. Chem. A* **2013**, *1*, 10662–10666; c) X. Li, S. Ding, X. Xiao, J. Shao, J. Wei, H. Pang, Y. Yu, *J. Mater. Chem. A* **2017**, *5*, 12774–12781.

[22] F. Zheng, Y. Yang, Q. Chen, *Nat. Commun.* **2014**, *5*, 5261–5261.

[23] K. Hong, L. Qie, R. Zeng, Z. Yi, W. Zhang, D. Wang, W. Yin, C. Wu, Q. Fan, W. Zhang, Y. Huang, *J. Mater. Chem. A* **2014**, *2*, 12733–12738.

[24] Y. Shao, J. Xiao, W. Wang, M. Engelhard, X. Chen, Z. Nie, M. Gu, L. V. Saraf, G. Exarhos, J. Zhang, *Nano Lett.* **2013**, *13*, 3909–3914.

[25] X. Zhou, Y. Guo, *ChemElectroChem* **2014**, *1*, 83–86.

[26] T. Zhai, H. Liu, H. Li, X. Fang, M. Liao, L. Li, H. Zhou, Y. Koide, Y. Bando, D. Golberg, *Adv. Mater.* **2010**, *22*, 2547–2552.

Manuscript received: June 13, 2017
Accepted Article published: July 16, 2017
Version of record online: August 4, 2017